Tephra Mass Eruption Rate From Ground-Based X-Band and L-Band Microwave Radars During the November 23, 2013, Etna Paroxysm

Frank Marzano, Luigi Mereu, Simona Scollo, Franck Donnadieu, Costanza Bonadonna

▶ **To cite this version:**

Frank Marzano, Luigi Mereu, Simona Scollo, Franck Donnadieu, Costanza Bonadonna. Tephra Mass Eruption Rate From Ground-Based X-Band and L-Band Microwave Radars During the November 23, 2013, Etna Paroxysm. IEEE Transactions on Geoscience and Remote Sensing, 2020, 58 (5), pp.1-14. 10.1109/TGRS.2019.2953167 . hal-02534691

HAL Id: hal-02534691
https://uca.hal.science/hal-02534691v1

Submitted on 30 Nov 2020

HAL is a multi-disciplinary open access archive for the deposit and dissemination of scientific research documents, whether they are published or not. The documents may come from teaching and research institutions in France or abroad, or from public or private research centers.

L'archive ouverte pluridisciplinaire **HAL**, est destinée au dépôt et à la diffusion de documents scientifiques de niveau recherche, publiés ou non, émanant des établissements d'enseignement et de recherche français ou étrangers, des laboratoires publics ou privés.

Distributed under a Creative Commons Attribution 4.0 International License

Tephra Mass Eruption Rate from Ground-based X-Band and L-Band Microwave Radars during the 23 November 2013 Etna Paroxysm

Frank S. Marzano, *Fellow, IEEE*, Luigi Mereu, Simona Scollo, Franck Donnadieu and Costanza Bonadonna

***Abstract*— In the morning of 23 November 2013 a lava fountain formed from the New South-East Crater (NSEC) of Mt. Etna (Italy), one of the most active volcanoes in Europe. The explosive activity was observed from two ground-based radars, the X-band polarimetric scanning one and the L-band Doppler fixed-pointing one as well as from a thermal-infrared camera. Taking advantage of the capability of the microwave radars to probe the volcanic plume and extending the Volcanic Ash Radar Retrieval (VARR) methodology, we estimate the mass eruption rate using 3 main techniques, named Surface-Flux Approach (SFA), Mass Continuity-based Approach (MCA) and Top-Plume Approach (TPA) as well as providing a quantitative evaluation of their uncertainty. Estimated exit velocities are between 160 and 230 m/s in the paroxysmal phase. The inter-comparison between the SFA, MCA and TPA methods, in terms of retrieved mass eruption rate, shows a fairly good consistency with values up to 2.4 10^6 kg/s. The estimated total erupted mass is 3.8, 3.9 and 4.7×10^9 kg for SFA with L band, X band and thermal-infrared camera, respectively. Estimated erupted mass is between 1.7×10^9 kg and 4.3×10^9 for TPA methods and 3.9×10^9 kg for the MCA technique. The SFA, MCA and TPA results for total erupted mass are in fairly good agreement with independent evaluations derived from ground collection of tephra deposit and estimated to be between 1.3 ± 1.1×10^9 and 5.7×10^9 kg. This study shows that complementary strategies of ground-based remote sensing systems can provide a real-time monitoring of a volcanic explosive activity.**

***Index Terms*—Volcanic plumes, Mass eruption rate, Total erupted mass, Microwave Doppler radar, Weather radar.**

Manuscript received on February 10, 2019. This work was supported by the European project EUROVOLC (H2020-INFRAIA-02-2017, Project n. 731070) "European Network of Observatories and Research Infrastructures for Volcanology".

F.S. Marzano and L. Mereu are with the Dipartimento di Ingegneria dell'Informazione, Elettronica e Telecomunicazioni (DIET), Sapienza Università di Roma, 00184 Rome, Italy, and also with the Center of Excellence CETEMPS, Università dell'Aquila, 67100 L'Aquila, Italy (e-mail: frank.marzano@uniroma1.it; luigi.mereu@uniroma1.it).

S. Scollo is with Istituto Nazionale di Geofisica e Vulcanologia, Osservatorio Etneo, Catania, Italy (simona.scollo@ingv.it)

F. Donnadieu is with the Observatoire de Physique du Globe de Clermont-Ferrand, Université Clermont Auvergne, France (franck.donnadieu@uca.fr).

C. Bonadonna is with the Department of Earth Sciences, University of Geneva, 1205 Geneva, Switzerland (e-mail: Costanza.Bonadonna@unige.ch).

I. Introduction

The characterization of the source parameters of explosive eruptions is of significant interest due to the environmental, climatic, and socioeconomic impact of tephra dispersal and sedimentation which might cause hardship and damages in areas surrounding volcanoes, including threat to aviation [9]. In particular, real-time monitoring of ash-rich plumes is also crucial for initializing volcanic ash transport and dispersion models [32], [13]. Tephra dispersal from an explosive eruption is a function of multiple factors, including mass eruption rate, degree of magma fragmentation, vent geometry, plume height, particle size distribution and wind velocity [43].

Mt. Etna, located on the east coast of Sicily (Italy) is one of the most active volcanoes in Europe. The most distinctive phenomena associated with the activity of Etna are represented by the volcanic plumes, sometimes characterized by a significant tephra discharge rate (e.g., [3], [1], [12]). Volcanic plumes at Etna mostly consist of sustained jets of fluid lava, propelled into the atmosphere from summit craters or lateral vents and driven by expanding gases, which commonly occur at basaltic volcanoes [7]. The fountain gains its momentum by the expansion of gas bubbles that exsolve from the magma as pressure falls while it is rising in the conduit. Height, duration and erupted volumes of Etna volcanic plumes can greatly vary, with strong lava fountains reaching a height of several hundreds of meters. On 23 November 2013 an intense explosive eruption formed from the NSEC and lasted for about an hour. This eruption has been widely analyzed in previous works, focusing on the eruptive processes and tephra volumes [3], integration of observational data [10], tephra fallout characterization [1], plume dynamics [36] and total grain-size distribution retrieval [38]. In this respect, few instrument-based estimates are available for the time series of the mass eruption rate, that is the amount of material erupted per unit time, a key parameter for evaluating hazard assessment and for ash plume dispersion model initialization [45], [4], [33], [34].

Near-real time mass eruption rate monitoring and estimation can be provided by several techniques: i) fixed-pointing Doppler microwave radar [24], [16], [20]; ii) optical imaging in clear-air conditions [46], [48]; iii) infrasound sensor network [39]; iv) electrical probing [6]. Most techniques are affected by significant uncertainties, with

considerable variations between different estimates of mass eruption rate [19]. Using a centimeter and millimeter wavelength, ground-based microwave radars represent an important tool for detecting and estimating near-source tephra mass eruption rate and concentration being their wavelength comparable or larger than size of lapilli and coarse ash particles as well as less affected by two-way extinction with respect to optical sensing [30], [50], [16].

Weather radar scanning systems can be exploited to monitor a volcanic plume, measuring the reflectivity due to small lapilli and coarse ash at a fairly high spatial resolution (less than a few hundred meters) and every few minutes [22], [26], [27], [28]. Weather radars can provide data for estimating the plume tephra volume, total mass and height, using the volcanic ash radar retrieval (VARR) for single-polarization and dual-polarization systems at S, C and X band [30], [31], [33]. Doppler fixed-pointing radars at L band has the antenna boresight typically oriented towards the volcano summit craters and are able to follow the plume column dynamics in near-real time providing both tephra power returns and Doppler velocities mainly due to lapilli and bombs [16], [17].

The aim of this work is to analyze the 23 November 2013 Etna volcanic plume in order to: i) extend the applicability of the VARR methodology to L-band Doppler radar for the quantification of mass eruption rate; ii) retrieve the incandescent region height and exit velocity from available polarimetric X-band radar data, Doppler L-band and thermal infrared camera; and iii) formulate mass eruption rate retrieval techniques in a unified way with their own uncertainty and estimate the mass eruption rate time series and total erupted mass. To reach this aim, we explore the application of three different strategies for the calculation of erupted mass based on near-surface flux, plume height and mass continuity, respectively, and we compare the associated results with those obtained from deposit-based techniques.

The paper is organized as follows. Section II briefly describes the available instruments as well the Etna eruption. Section III shows the proposed methodology to derive the tephra mass eruption rate and erupted mass. The radars and camera data set is presented in Section IV together with the discussion of the results. Conclusions are presented in Section V.

II. Case Study and Data

The Istituto Nazionale di Geofisica e Vulcanologia, Osservatorio Etneo (INGV-OE) is equipped with a large set of instruments installed for real-time monitoring of the Etna eruptive activities [41]. Various sensors are included at the Etna site such as several seismic and acoustic sensors, two optical lidars, microwave radars, thermal infrared and visible cameras, installed at different times during the INGV-OE instrument site expansion (e.g., [41], [48]). The Dipartimento della Protezione Civile (DPC) of Italy operates an X-band mobile weather radar installed at the Catania airport [36], [50].

A. Mt. Etna eruption on 23 November 2013

The 23 November 2013 episode represents one of the most explosive events among all the lava fountains that have occurred at Etna from 2011 to 2013 [41], [1]. The eruption started with a Strombolian activity in the afternoon of the day before. The activity moved from Strombolian to volcanic plume after 9:30 UTC and formed an eruption column that grew suddenly and reached the height of 11 km above sea level (asl) during the most intense phase [10]. The thick volcanic plume and cloud spread tephra particles up to several hundreds of kilometers from the summit craters toward the north-east direction [3]. The volcanic plume portion, characterized by the hot jet made also by coarse pyroclasts [1], was clearly distinguishable from the higher eruptive column governed by buoyancy. Abundant fallout of bombs and coarse lapilli occurred on the lower north-east flanks of the volcano, while fine lapilli dispersed all along the Ionian coast of Sicily. The fallout of clasts of several tens of centimeters caused severe damage to buildings, solar panels, and cars, and injured a few hikers about 5 km from the crater [1].

This volcanic plume was clearly observed from the X-band polarimetric weather radar and L-band fixed-pointing Doppler radar as well as from a visible and a thermal-infrared camera of the INGV-OE surveillance system. For this case study the map of **Fig. 1** shows the location of the remote sensing instruments used in this study, whose main characteristics are briefly listed here:

1) the X-band Microwave Weather Radar (MWR) dual-polarization scanning radar, included in the Italian weather radar network [50]. The dual use of X-band MWR for the detection of both meteorological and volcanic clouds is possible thanks to a combination of several factors: wavelengths of about 3.1 cm (frequency of 9.6 GHz), transmitted peak power of 50 kW, half-power beamwidth of 1.3° and permittivity factor of ash particles (equal to 0.39 with respect to 0.93 of water particles) [29], [35]. The X-band MWR performs a 3-dimensional scan of the surrounding scene as a function of range, azimuth and elevation with 5 antenna rounds per minutes. The X-band MWR acquisitions consist of data volumes having an area of about 160x160 km^2 wide and 20 km tall. The data volume cross-sections are sampled along 12 elevations angles plus a vertical one, as shown in **Fig. 1**, and released every 10 minutes at a distance from the NSEC of about 32 km. The MWR volume, scanned near the NSEC, has a range resolution of 200 m and about 700x700 m^2 transverse spatial resolution.

2) the ground-based L-band Doppler radar (VOLDORAD-2B or VDR hereinafter), operating at a wavelength of 23.5 cm (frequency of 1.274 GHz) was designed by the Observatoire de Physique du Globe de Clermont-Ferrand (OPGC) for the monitoring of explosive activity [16], [17]. It can be deployed near an eruptive vent to measure in real-time the eruptive velocities and backscattered power at high rate up to 20 s^{-1}. The VDR signal wavelength allows to sound dense lava jets and ash-laden plumes as well as to avoid attenuation by hydrometeors because of cloudy, foggy, rainy, or snowy conditions. Owing to its modularity and limited weight (about 70 kg) the ensemble is easily transportable and, thus, can be used for short-term scientific campaigns, as well for long-term monitoring. At Etna, VOLDORAD-2B is jointly operated

by INGV-OE and OPGC, sounding (fixed pointing) 13 volumes (about 28×10^8 m^3) right above the summit craters every 0.23 s. Its capacity to provide first-order mass eruption rate (MER) in real-time, as well as total erupted mass (TEM), onset and end of volcanic plumes, and eruptive crater has recently been shown [17]. Processed velocity and echo power data are stored in an open access data base made available from the OPGC website and EPOS platform (see the Acknowledgement later on).

3) the Thermal-Infrared Camera (TIC) is located at ~15 km southward from the craters and belongs to the INGV-OE network of video-surveillance system. TIC provides a time series of 640×480 pixel images with a spatial resolution of few meters considering the distance between the TIC and the NSEC crater [3], [7]. The height, width and area of the volcanic plume can be detected by properly selecting the saturated portion of the measured brightness imagery and adopting the procedure described in [15] and [3].

B. Sensor data processing

MWR, VDR and TIC can be processed to derive useful near-source variables. VDR can provide an estimate of the exit velocity v_{ex}, whereas the incandescent region height can be retrieved from MWR and TIC. From both VDR and MWR an estimate of tephra concentration, mean diameter and mass eruption rate can be also derived using the VARR algorithm.

1) MWR data processing. The polarimetric MWR is capable to measure not only the X-band copolar horizontally-polarized reflectivity factor Z_{hh} (hereinafter very often simply called reflectivity), but also other polarimetric moments such as the differential reflectivity Z_{dr}, differential phase shift K_{dp} and the copolar correlation coefficient r_{hv} (elsewhere also indicated by ρ_{hv} or ρ_{co}) [29], [50]. **Fig. 2** shows the vertical profiles of X-band Z_{hh}, Z_{dr}, K_{dp},and r_{hv} along the line connecting the radar antenna with horizontal maximum expansion of the plume (see [36] and [50] for similar plots). It is interesting to note the contrasting trend of X-band Z_{hh} and r_{hv} in the areas immediately above the crater extending vertically for a few kilometers. The X-band Z_{hh} reaches a maximum altitude of 11 km asl, decreasing horizontally more severely after about 20 km from the summit craters, probably due to a faster fallout of large particles, a region identified by values of $Z_{hh}\geq$50 dBZ. The area with low X-band reflectivities ($Z_{hh}<$30 dBZ) is associated with outermost edges of the plume suggesting the presence of coarse particles prone to fallout in agreement with the tephra sampling [1]. Since r_{hv} measures the consistency of copolar signal power and phase for each received pulse pair, r_{hv} confirms the Z_{hh} trend, revealing a fairly apparent vertical separation between the incandescent saturated region and the convection eruptive region just above [50]. The Z_{dr} signatures is relatively low, oscillating around 0.02-0.005 dB, meaning that tephra particles are detected as spherical on average (the material injected from the crater is still very fluid and is characterized by some degree of anisotropy, as noted in [32]. The K_{dp} signature shows an increase in a region which is slightly displaced with respect to the column above the crater. Positive values of K_{dp} typically indicate slightly horizontal orientation for oblate volcanic particles. The behavior of K_{dp} increment could be due to the presence of falling large lapilli and bombs with a ballistic trajectory.

Fig. 3 shows the maximum values of both X-band MWR Z_{hh} and r_{hv} along the column closest to the NSEC at about 32 km using the fourth elevation angle (see Figs. 1 and 2). This plot can be interpreted by looking at the vertical profile of Fig. 2. In particular, low values of r_{hv} suggest non-spherical shapes and tumbling of volcanic particles [29] so that in Fig. 3 the region with $r_{hv}<$0.95 can be divided into two regions where different physical processes are probably occurring [36]: (a) the region above the NSEC, where the ascending gas and particles form the eruption column that is progressively inclining and thickening as it propagates downwind; (b) the region, aside the NSEC at horizontal distances less than about 5 km from the crater, which can be reasonably associated with the fallout of irregular large lapilli and bombs. The region, having $r_{hv}>$0.95, extends over the entire remaining plume, detected by the X-band MWR, thus including both lateral cloud advection by wind and fallout of tephra particles [36].

From Fig. 3 it emerges that a combined thresholding on both X-band MWR Z_{hh} and r_{hv} can be used to detect the incandescent region height H_{IR}. In this case study, by doing an iterative analysis aimed at finding a relatively stable estimate, we have empirically set the combined condition $Z_{hh}\geq$50 dBZ and $r_{hv}<$0.95 to retrieve H_{IR}. From C band polarimetric observations of the 2012 Mount Tongariro, for a tephra plume associated to a more viscous magma than Etna, a transition at r_{HV} around 0.9 has been found corresponding to a stronger decrease of reflectivity upward about 1 km above the vent. This limit reflects the upward transition to the buoyancy-dominated convective column that rose about 5 km high.

Indeed, we should have a larger set of explosive eruptions, observed by a polarimetric radar, but so far the paroxysm on 23 November 2013 remains one of the best case studies at Etna where the H_{IR} signature is quite clean in both r_{HV} and Z_{hh} signal. This approach may be probably improved by including the other polarimetric features in a tree-logic approach, but from the case study of 23 November 2013 it seems that the improvement is relatively negligible. The relatively good agreement of the proposed radar-based H_{IR} retrieval algorithm with the estimates from thermal infrared camera supports the current approach. Note that, due to MWR finite antenna beam width and the distance of 32 km from the summit craters, the spatial cross-resolution along the eruption column is about 700 m (see Fig. 1).

2) VDR data processing. The fixed-pointing L-band VDR is measuring both the radial velocities v_r and the received backscattered power P_{RX} derived from L-band VDR [16]. From the observation geometry we can convert v_r into exit velocity v_{ex} normal to the surface of summit craters (i.e., v_{ex} = 3.89 v_r) [17], whereas from the specifications of the L-band VDR and the radar constant, the backscattered power P_{RX} can be transformed into the L-band horizontally-polarized reflectivity factor Z_{hh}. **Fig. 3** shows the VDR Z_{hh} corresponding to its third or fourth range bin, acquired every about 17 s and down-sampled every 10 min in order to reconcile the time sampling with that of MWR. The time-trend of Z_{hh} is related to the VDR range gate closest to the NSEC.

The VDR radar reflectivity factor is higher by 15 dBZ with respect to MWR during climax at 10:00 UTC. This may be due to sampling location mismatches, VDR being measuring right above the crater, effects of Mie scattering regime and impacts of particle non-sphericity, affecting the incandescent region above the crater dominated by bombs and lapilli in the proximal fallout region.

3) TIC data processing. The TIC measurements can be processed to extract the incandescent region height H_{IR} from the recorded thermal-infrared brightness temperature imagery over the eruptive time interval [3]. Most techniques are based on imposing a proper threshold to the vertical spatial gradients and/or to edge-contour detection filters [15]. Selecting the TIC frames at time intervals of 1 min, it is possible to derive the incandescent region height H_{IR} in each image.

4) Tephra concentration. Starting from Z_{hh} derived from both X-band and L-band radars, we can apply the VARR methodology, considering the ad hoc physical-electromagnetic model of non-spherical ash particles in order to derive the mean sphere-equivalent diameter D_n and the tephra mass concentration C_t (also denoted as C_a in [26]: here we prefer the notation C_t dealing with near-source pyroclats). The latter is defined as [26]:

$$C_t = \int_0^\infty \left(\frac{\pi}{6}\right) D^3 \rho_t(D) N_t(D) dD = \rho_t \, f_N(D_n, \mu, N_n) \quad (1)$$

where D is the sphere-equivalent diameter (mm), ρ_t is the volcanic particle specific density (kg/m^3), N_t is the particle size number distribution (PSD, in m^{-3} mm^{-1}), typically characterized by 3 parameters (i.e., mean diameter D_n, shape parameter μ and number concentration N_n) [26]. The volcanic particle size distribution is parametrized using field and combined data [38]. (1) holds if ρ_t is constant and introduces the *airborne-particle volumetric fraction* f_N providing, as a function of PSD parameters, the fraction of tephra particles per unit volume or, more generally, the degree of rarefaction of the ejected material. From (1) percentage values of f_N for tephra are usually less than 0.01% [29]. The extension of VARR to L band is quite straightforward as the backscattering model is valid for both Rayleigh and Mie regimes and the considered particle sizes range from 64 μn up to 32.768 mm.

5) VARR processing. **Fig. 4** shows the VARR-based maximum and minimum retrievals of C_t and D_n, obtained from X-band MWR and L-band VDR data in the range gate nearest to the NSEC (see Fig. 3). The mass concentration retrievals can reach values of 18 g/m^3 for L-band VDR and 7 g/m^3 for X-band MWR, whereas mean-diameter estimates show sizes from about 5.0 to 12 mm for L-band VDR and from 0.1 to 4 mm for X-band MWR. Interestingly, the modal diameter of proximal lapilli sampled immediately near the cone for the July 2011 Etna paroxysm was between 11 and 16 mm [7]. Consistently with the radar wavelength, L-band VDR is mainly sensitive to lapilli and bombs, whereas X-band MWR response is also influenced by smaller coarse particles [29]. It is worth noting that MWR peaks (around 10:00 UTC) are slightly anticipate with respect to VDR ones (around 10:10 UTC). Assuming a particle density ρ_t of 2700 kg/m^3, airborne-particle volumetric fraction f_N is typically less than 10^{-7}.

III. Estimating Mass Eruption Rate

The main goal of this work is to provide an estimate of mass eruption rate using MWR, VDR and TIC showing how their retrievals can be processed using a unified approach. Indeed, the capability of ground-based radars to estimate the time-dependent Mass Eruption Rate (MER), here also indicated by the symbol $Q_M(t)$, is still an open issue [33], [31], [50].

From a methodological point of view, the time-dependent mass eruption rate $Q_M(t)$ can be related to the plume top height H_{TP} and to incandescent region height H_{IR}. Note that the incandescent region height may be similar or higher that the gas-thrust region height (depending on the eruption style where the fragmented particle momentum is coupled or not with tephra plume jet [43]). In this respect, we can apply 3 approaches in order to estimate $Q_M(t)$: 1) the Surface Flux Approach (SFA), physically relating $Q_M(t)$ to the eruptive exit velocity v_{ex}, tephra density and the geometry of the crater; 2) Top Plume Approach (TPA), using semi-empirical parametric models considering the top plume altitude and environmental parameters; the Mass Continuity Approach (MCA), using the mass continuity equation within the erupted plume above the crater.

A. Methods

1) Surface Flux Approach (SFA). The tephra mass eruption rate Q_M(t) (kg/s) (sometimes also indicated by $\dot{M}(t)$) through the crater at each instant time t can be written as:

$$Q_M^{(SFA)}(t) = \int_{S_v} \rho_x(x,y,t)\; v_{ex}(x,y,t) dS_v \cong \rho_x(t)\; v_{ex}(t)\; S_v \quad (2)$$

where the crater has a surface S_v (m^2) in (x,y) coordinates, ρ_x (kg/m^3) is the density of the eruptive mixture and v_{ex} (m/s) is the vertical exit velocity normal to the crater surface. In the right-hand side of (2) we assume that both ρ_x and v_{ex} are constant averaged values within S_v, a reasonable assumption if the crater is relatively small. The objective of the SFA approach, in order to retrieve the time series of $Q_M(t)$, is to provide an estimate of ρ_x, v_{ex} and S_v from remote sensing instruments MWR, VDR and TIC at each instant time t, as it will be discussed in the following text.

In order to estimate ρ_x in (2), we can consider that Etna volcanic plumes are typically characterized by gas fractional content f_g between 2% and 3% [8], a gas density ρ_g between 0.10 and 0.20 kg/m^3 and a magma density ρ_m between 2500 and 3000 kg/m^3 [46]. These values result in a fragmented magma-gas mixture density ρ_x at the vent given by:

$$\rho_x = \frac{\rho_m \rho_g}{\rho_m f_g + \rho_g f_m} = \frac{\rho_m \rho_g}{\rho_m f_g + \rho_g (1 - f_g)} \quad (3)$$

where f_m is the volumetric fraction of magma, holding in the right-hand side of (3) a linear mixing with f_m=1-f_g [48]. In order to get estimates of ρ_x from (3) (e.g., [8], [48]), by considering volcanic gas is mainly due to water vapor with ρ_g=0.15 kg/m^3, assuming ρ_m=2700 kg/m^3 and f_g=0.01, from (3) we get ρ_x=14.9±3.0 kg/m^3. Note that, if f_g=0.020 and ρ_g=0.10 kg/m^3 (low gas fraction and density), then ρ_x=7.0 kg/m^3, whereas if f_g=0.03 and ρ_g=0.20 kg/m^3 (high gas fraction and

density), then ρ_x=5.0 kg/m^3, but if f_g=0.02 and ρ_g=0.20 kg/m^3 (low gas fraction with high density), then ρ_x=10.0 kg/m^3.

In order to estimate S_v in (2), we can adopt the usual assumption of a cylindrical conduit with a circular crater with an area $S_v=\pi r_v^2$, being r_v the radius [39]. Experimental evidences suggest the radius can be set to 13.5 m with an uncertainty of ~10% [8], [7], a value which reinforces the approximation of constant ρ_x. This radius estimate is confirmed by the inspection of the available thermal-infrared imagery evaluating the average size of the detected vertical column. An estimate of S_v is then about 572.5±57.0 m^2.

In order to estimate v_{ex} in (2), we should distinguish between the 3 sensors: L-band VDR provides directly v_{ex} as a normal projection of the measured Doppler radial velocity v_r, whereas both X-band MWR and TIC data can provide an estimate of the incandescent region height H_{IR} (see Sect. II.B). Indeed, X-band MWR is a Doppler radar and velocity profiles can be also estimated from ad hoc data processing [36]. However, as pointed out in [36], radar estimate of the updraft velocity cannot be considered as an exit velocity but is rather its proxy. This is the reason why in this work we explore the use of the MWR-based estimate of the incandescent region height. The latter can be used to retrieve v_{ex} based on to the ballistic equation, also known as Torricelli's equation [45], [40]. This equation, also deducible from energy conservation, can provide an estimate of H_{IR} associated to the vertically-directed outflow velocity v_{ex} of a pyroclastic constant flow from the volcano crater, and vice-versa, at each instant time t through:

$$\begin{cases} v_{ex}(t) = \sqrt{2\,g\,H_{IR}(t)} \\ H_{IR}(t) = v_{ex}^2(t)/2\,g \end{cases} \tag{4}$$

where g (m/s^2) is the Earth gravity acceleration and the atmospheric density variation and drag effects are considered to be negligible within the incandescent region. This expression is a valid approximation within the incandescent region, when most pyroclasts are sufficiently large to be considered uniformly accelerated projectiles not entering into the upper convection region of the plume [45]. This is typically the case for ballistic bombs. Note that, due to the non-linear relation present in (4), for a H_{IR} of 2000 m, an uncertainty of 20% (400 m) reflects into an uncertainty of 10% on v_{ex} (19.7 m/s).

The use of (4) together with (3) and (2) allows the SFA-based estimate of tephra mass eruption rate from both X-band MWR and TIC data. The overall percentage uncertainty ε_Q of the approximate mass eruption rate $Q_M(t)$ in (2) can be estimated using the first-order error propagation theory for independent (maximum) errors, obtaining the following expression:

$$\varepsilon_Q^{(SFA)} = \frac{\delta Q_M{}^{(SFA)}}{Q_M} = \sqrt{\left(\frac{\delta\rho_x}{\rho_x}\right)^2 + 4\left(\frac{\delta r_v}{r_v}\right)^2 + \frac{1}{4}\left(\frac{\delta H_{IR}}{H_{IR}}\right)^2} \tag{5}$$

where $\delta\rho_x$, δr_v and δH_{IR} are the (maximum) errors on density at the crater, circular radius and incandescent region height that are causing the overall error δQ_M on the mass eruption rate. If from previous considerations we assume that $\delta\rho_x=0.15\rho_x$, $\delta r_v=0.10 r_v$ and $\Delta H_{IR}=0.20 H_{IR}$, the relative percentage error $\varepsilon_Q{}^{(SFA)}$=26.9%. Note that if the errors are Gaussian distributed, then their standard deviation $\sigma_{QM\text{-}SFA}$ is 33% of the maximum error $\delta Q_{M\text{-}SFA}$.

2) Mass continuity approach (MCA). The mass continuity equation can be applied to estimate the mass eruption rate [33], [31]. The mass eruption rate can be decomposed into 2 terms, first one $Q_{Mdif}(t)$ related to the time-variation of the tephra mass M_t between two adjacent instants within the erupted volume and the second one $Q_{Madv}(t)$ related to the advection of tephra mass with a vector velocity **v** through the erupted volume. In formula [33]:

$$Q_M^{(MCA)}(t) = Q_{Mdif}(t) + Q_{Madv}(t) = \frac{\partial M_t(t)}{\partial t} + \oint_S C_t(\mathbf{r},t)[\hat{\mathbf{n}}_S(\mathbf{r},t)\cdot\mathbf{v}(\mathbf{r},t)]dS \tag{6}$$

where M_t is the tephra mass within the volume enclosed within the closed plume surface S detected by the weather radar scan, C_t is the tephra mass concentration, **r** is the range vector, $\hat{\mathbf{n}}_S$ is the unit vector normal to the surface S and **v** is the tephra velocity field. The advection term in (6) can be estimated either by the Doppler field, even though radial velocities should be transformed into vector velocity with arbitrary assumptions, or by a space-time cross-correlation technique providing only a single displacement vector for the detected tephra volume [33], [31]. The contribution to the mass eruption rate of the advection term $Q_{Madv}(t)$ is generally much less than the other term related to time-derivative of the tephra mass.

To estimate the mass eruption Q_M in (6), the input data is the time series of $Q_{Mdif}(t)$ and $Q_{Madv}(t)$ provided by scanning weather radar such as X-band MWR. As already discussed for SFA uncertainty, the overall percentage uncertainty $\varepsilon_{Q\text{-}MPA}$ of $Q_M(t)$ in (6) can be estimated by:

$$\varepsilon_Q^{(MCA)} = \frac{\delta Q_M{}^{(MCA)}}{Q_M} = \sqrt{\left(\frac{\delta Q_{Mdif}}{Q_M}\right)^2 + \left(\frac{\delta Q_{Madv}}{Q_M}\right)^2} \tag{7}$$

where δQ_M is the mass eruption rate (maximum) error. If we assume that $\delta Q_{Mdif}=0.20 Q_{Mdif}$ (due to error in tephra volume and time undersampling) and $\delta Q_{Madv}=0.10 Q_{Madv}$ (due to errors in velocity field estimation), the relative percentage error $\varepsilon_{Q\text{-}MCA}=(\delta Q_M/Q_M)$=22.3%.

3) Top-plume approach (TPA). Numerical 1-dimensional (1-D) models, theoretical simplified models and field-based empirical relationships relate the top-plume height H_{TP} to the instantaneous tephra mass eruption rate $Q_M(t)$ through a generalized power law [51], [52], [43], [45], here expressed in a compact form as:

$$Q_M{}^{(TPA)}(t) = a_0\,H_{TP}{}^b(t) + a_1\,H_{TP}{}^c(t) \tag{8}$$

where the coefficients a_0, a_1, b, and c are properly set either by experimental fitting or model analyses.

In particular, in this work we have considered the following estimators of mass eruption rate:

- the empirical relationship, proposed by [32] and here named TPA-MA09, where in (8) a_1=0 and c=0, whereas a_0=3.29 kg/s/m^b and b=4.15. Note that TPA-MA09 is indeed proposed in terms of volumetric eruption rate, expressed in m^3/s, and here has been converted into mass eruption rate by assuming a magma density ρ_m=2500 kg/m^3 as prescribed in [32].
- the analytical relationship, proposed by [13] and here named TPA-DB12, where b=4, c=3 and the coefficients a_0 (kg/s/m^b) and a_1 (kg/s/m^c) are dependent on the air/plume density and temperature, specific heat capacity, mean buoyancy frequency, radial/wind entrainment and mean wind velocity across the plume height [13]. In this case study, the considered value of the mean cross-wind along the plume maximum vertical extension is about 20 m/s, using the local model weather forecasts [41].

To estimate the mass eruption rate Q_M in (8), the input data is the time series of top-plume height $H_{TP}(t)$ which can be provided by visible cameras, satellite data and a scanning weather radar (e.g., [10]). As already discussed for SFA uncertainty, the overall percentage uncertainty $\varepsilon_{Q\text{-}TPA}$ of $Q_M(t)$ in (8) can be estimated by:

$$\varepsilon_Q^{(TPA)} = \frac{\delta Q_M{}^{(TPA)}}{Q_M} = \sqrt{\left(\frac{\delta a_0}{a_0}\right)^2 + \frac{1}{4}\left(\frac{\delta H_{TP}}{H}\right)^2} = \frac{a_0\, b H_{TP}{}^{b} + a_1 c\, H_{TP}{}^{c}}{a_0\, H_{TP}{}^{b} + a_1\, H_{TP}{}^{c}} \frac{\delta H_{TP}}{H_{TP}} \tag{9}$$

where δQ_M is the mass eruption rate (maximum) error. If for MA09 we assume that $\delta a_0 = 0.20 a_0$ and $\delta H_{TP} = 0.20 H_{TP}$, the relative percentage error $\varepsilon_Q^{(TPA)} = (\delta H_{TP}/H_{TP}) = 83.0$ %. For large volcanic eruptions this uncertainty has been recently quantified **Errore. L'origine riferimento non è stata trovata.**.

B. Total erupted mass

In summary, the instantaneous mass eruption rate $Q_M(t)$ is obtained:

- for SFA, from (2) after deriving $v_{ex}(t)$ directly from L-band VDR and through H_{IR} in (4) from X-band MWR and TIC, assuming estimates of ρ_v=14.9 kg/m^3 and S_v=572,5 m^2;
- for MCA, from (6) the mass eruption rate can be derived known the time-derivative mass flux and advection-related flux.
- for TPA, from (8) after deriving h_{TP} from X-band MWR data.

Once knowing the time series of the mass eruption rate $Q_M(t)$ by means of the SFA and TPA methods, by integrating them along whole time interval Δt of explosive eruption, we can compute the time-integrated erupted mass $M_I(t)$ (kg), the total erupted mass M_T (kg) as well the dense-rock-equivalent (DRE) total erupted volume V_T (m^3):

$$\begin{cases} M_I(t) = \int_0^t Q_M(t')dt' \\ M_T = \int_{\Delta t} Q_M(t)dt = M_I(t = \Delta t) \\ V_T = \int_{\Delta t} Q_V(t)dt = \int_{\Delta t} \frac{Q_M(t)}{\rho_m} dt = M_T/\rho_m \end{cases} \tag{10}$$

where Q_V (m^3/s) is the DRE eruption rate, given by the mass eruption rate divided by the magma density ρ_m, and Δt the event duration. Note that $M_I(t)$ expresses the mass erupted till a given time t starting from the eruption onset, whereas M_T is the total mass erupted during the whole event. The latter M_T is converted into V_T through magma density ρ_m. The total erupted volume is introduced to allow a straightforward comparison with results available in literature on the same case study.

As previously discussed, all methods SFA, MCA and TPA are affected by uncertainties and so is the total erupted mass M_T. If we assume that the Q_M error fraction ε_f for each method is time invariant, it can be easily shown that the erupted mass fractional error is given by:

$$\varepsilon_{TEM} = \frac{\delta M_T}{M_T} = \sqrt{\frac{\delta(\sum_i Q_M(t_i)\Delta t)^2}{(M_T)^2}} = \sqrt{\frac{\left(\sum_i \varepsilon_f Q_M(t_i)\right)^2}{(\sum_i Q_M(t_i))^2}} = \varepsilon_f \tag{11}$$

where t_i are the sampling time instant and Δt is the time step.

Note that the time series of the mass eruption rate $Q_M(t)$ and volumetric eruption rate $Q_V(t)$ is sometimes summarized by the time-averaged mass eruption rate $\bar{Q}_M$ and volumetric eruption rate $\bar{Q}_V$ [3], [1]. In our notation they are defined as:

$$\begin{cases} \bar{Q}_M = \frac{1}{\Delta t}\int_{\Delta t} Q_M(t)dt = \frac{M_T}{\Delta t} \\ \bar{Q}_V = \frac{1}{\Delta t}\int_{\Delta t} Q_V(t)dt = \frac{V_T}{\Delta t} \end{cases} \tag{12}$$

where Δt is the event duration. $\bar{Q}_M$ and $\bar{Q}_V$ are, indeed, the time-average of M_T and V_T, respectively, that is the total erupted mass and volume divided by the event duration Δt.

IV. Results

Once defined the SFA, MCA and TPA methodologies in the previous section, we can apply them to estimate the mass eruption rate and its derived parameters in (10) and (12) for the case study of the 23 November 2013 Etna volcanic plume.

SFA-based techniques are dependent on the estimate of the tephra exit velocity at the crater, derived from each available sensor. **Fig. 5** shows estimates of the exit velocity v_{ex} directly derived from of L-band VDR, as well as those derived from X-band MWR and TIC data using H_{IR} and (4). Estimated exit velocity v_{ex} shows a behavior similar to H_{IR} with a maximum at 10:00 UTC with values around 240 m/s from L-band VDR, 230 m/s from TIC data and 235 m/s from X-band MWR. Fig. 5 also shows estimates of H_{IR} directly derived from of X-band MWR and TIC data as well as those derived from L-band VDR using v_{ex} and (4). The maximum H_{IR} is reached at 10:00 UTC, which for the L-band VDR is around 2600 m above the crater level (acl), for the TIC data around 2500 m acl and for the X-band MWR around 2550 m acl. These H_{IR} estimates are consistent in terms of both values and trends.

In the left panel (a) of **Fig. 6** the time series of the retrieved mass eruption rate Q_M (t) are shown, sampled every 10 minutes (the lowest temporal sampling due to the X-band radar), using SFA, TPA and MCA methods from TIC data, X-band MWR and L-band VDR. The TPA method, based on the DB12 parametric model, uses an average wind velocity of 20

m/s averaging the vertical wind profile inside the eruption column).

Mass eruption rate estimates from all sensors are in a fairly good agreement in the paroxysmal time step from 09:50 till 10:20 UTC with maximum values between 1.0×10^6 and 2.3×10^6 kg/s. At the beginning of the eruption L-band VDR and TIC data tend to provide mass eruption rate estimates higher than X-band MWR ones, the latter probably being affected by the uncertainties in H_{IR} discrimination due to a relatively poor cross-correlation coefficient ρ_{hv} signal as well as to the low transverse resolution of the radar beam. At the climax of the eruptive episode all retrievals methods are in a fairly good agreement, the TIC-based mass eruption rate being the largest. The impact of wind velocity on DB12 model tend to provide a mass eruption rate which is slightly higher (about 25% more) than SFA-based ones. On the other hand, the MCA-based approach is very close to the DB12 estimates during the paroxysm climax, probably due to the similar approach based on the erupted plume features such as the plume top height (for TPA) or airborne plume mass (for MCA). As expected for bent-over plumes, the MA09 strategy tends to underestimate the mass eruption rate with respect to the other methods due to strong wind advection; such an effect is taken into account into DB12 TPA-based method.

Mass eruption rate estimates can be used to evaluate the accumulated ejected mass during the eruption temporal evaluation. The right panel (b) of **Fig. 6** also shows the time-integrated erupted mass $M_I(t)$ in (10) using the same methods as shown in Fig. 6(a), i.e. SFA and MCA from X-band MWR, L-band VDR and TIC data as well as TPA from DB12 and MA09. In this plot the total erupted mass M_T is represented by value at the last time step at 10:40 UTC, as deducible from (9). Where mass eruption rate starts to decrease around 10:10 UTC, $M_I(t)$ values tend to saturate. Indeed, from (10), the last value at 10:40 UTC of $M_I(t)$ provide the erupted mass retrieved values between 3.6×10^9 kg/s from VDR up to 4.7×10^9 kg/s from TIC data, except for MA09 (1.7×10^9 kg/s) affected by more uncertainty (estimated to be factor of about 50 at 95% [20]). Note that at the beginning of the volcanic eruption around 9:30 UTC, VDR seems to have already detected some extra mass rate which could be added to values here reported [20].

The uncertainty of each mass eruption rate estimation technique, introduced in (5), (7) and (9), can suggest the confidence interval of the obtained results. **Fig. 7** shows the trend of the mass eruption rate estimated value and the respective uncertainty for all methods (SFA, TPA and MCA) at each sampling time. Between 09:50 and 10:10 UTC, that is the interval of the largest eruptive activity, the uncertainties (error bars) are, in general, bigger. SFA method estimates show a more significant departure, even considering their uncertainty, within the ending tail of the eruption, a feature probably related to the uncertainty in the use of the Torricelli equation (to estimate of incandescent region height or exit velocity, as shown in Fig. 5) and the summit crater which may even change within the eruption itself. The two DB12-based and MA06-based TPA methods show an expected discrepancy which is not accounted for their relative uncertainties. MCA-based values have uncertainties comparable to DB12-based ones. Finally, the average and standard deviation of all-method retrieved mass eruption rates shows an overall fairly consistent increasing and decreasing trend with a paroxysm mass eruption rate standard variability between 1.5 and 2.4×10^6 kg/s.

In most cases the only way to validate mass eruption rate estimates is to compare the total erupted mass, derived from mass eruption rate, with available ground deposits. The estimates of the total erupted mass M_T (kg) is shown in **Table I** for the 23 November 2013 Etna volcanic plume. The results refer to erupted mass derived from literature data (see rows *a*, *b* and *c1* and *c2*) together with TPA-MA09 and TPA-DB12 estimates (see rows *d* and *e*), SFA retrievals from TIC data, X-band MWR and L-band VDR (see rows *f*, *g* and *h*) and X-band MWR MCA (see row *i*), respectively. Uncertainties, estimated by (5), (7) and (9), are also indicated. All retrievals show the same order of magnitude around few ktons in agreement with the erupted mass derived from satellite data (3.0×10^9 kg in *b* and 5.7×10^9 kg in c_1) as well from wind-driven TPA-DB12 (4.3×10^9 kg in *d*). The SFA estimates are interestingly very similar among them with estimates 3.8×10^9 kg (from L-band VDR) and 4.7×10^9 kg (from TIC data). These mass eruption rate retrievals are within the uncertainty of the 23 November 2013 Etna eruption field values (see rows *a* and c_1) providing erupted mass values between $1.3\pm1.1\times10^9$ kg and 5.7×10^9 kg, obtained by estimating the fallout deposit using the Weibull distribution [1], [38]. Moreover, they are higher than TPA estimates from MA09 with a erupted mass of 1.7×10^9 kg, but in fairly good agreement with DB12 and MCA ones showing values around 4.3 (with mean wind velocity of 20 m/s) and 3.9 $\times10^9$ kg, respectively.

Independent estimates of time-average mass and volumetric rates can be also used for comparison [1], [3]. Using a magma density ρ_m=2700 kg/m^3 [8] and Δt=4200 s (70 minutes, from Fig. 6a), **Table II** shows erupted mass and volumetric eruption rates, computed as defined in (10) and (12), from SFA methods using TIC data, X-band MWR and L-band VDR, from X-band MWR MCA method and derived from literature. As expected from the discussion on erupted mass estimates, the 3 SFA retrievals are in good agreement with time-average mass eruption rates between 1.6 and 0.9×10^6 kg/s, time-average volumetric discharge rates between 627 and 335 m^3/s and dense-rock-equivalent volumes between 1.9 and 1.4 10^6 m^3. The lowest values are shown in MCA approach but similar that reported in [1]. By assuming ρ_m=2700 kg/m^3 (accepting an uncertainty of 10%) and Δt=3000 s (50 minutes, disregarding the first and last 10 minutes), SFA-based time-average volume discharge rates are between 627 and 335 m^3/s, the latter value close to 360 m^3/s as reported in [3] using an estimate based on a thermal-infrared camera for the same event. The MCA-based time-averaged volumetric eruption rate is characterized by a value between 348 and 526 m^3/s. The total erupted volumes, derived from SFA methods, are in a fairly good agreement with those provided in [3] and in [20] of 1.6-1.7 10^6 m^3.

V. Conclusion

Three different approaches have been presented and compared to determine mass eruption rate from microwave radars at L band (23.5 cm wavelength) and X band (3.1 cm

wavelength), namely the surface-flux approach (SFA), the mass-continuity approach (MCA) and the top-plume approach (TPA). These approaches exploit the radar Doppler or polarimetric capabilities as well as fixed-pointing or scanning mode and both radar data have been processed by means of the model-based volcanic ash radar retrieval (VARR) methodology. We have also discussed the overall formulation and some assumptions behind both SFA and TPA methods, showing how these uncertainties can reflect into the estimate of the total erupted mass as well as time-average discharge rates. As a reference we have taken into account the estimate of the mass eruption rate from a video thermal-infrared camera (TIC), exploiting its capability to detect the gas- thrust region height in this event and applying the Torricelli equation to estimate the exit velocity. The latter, when estimated from X-band MWR, L-band VDR and TIC data, are between 160 and 230 m/s in the paroxysmal event within a difference among the various sensor retrievals less than 25%.

The inter-comparison between the SFA and TPA methods, in terms of both mass eruption rate and erupted mass, shows fairly good agreement. Estimated erupted mass is between 3.7 and 3.8×10^9 kg for SFA applied to L and X band radar data, respectively, and between 1.7 and 4.7 x 10^9 kg based for TPA, slightly less than the camera-based estimates equal to 4.7 x 10^9 kg. MCA-based erupted mass estimates are comparable to SAF ones. These SFA, MCA and TPA results for erupted mass are in good agreement with the tephra fall deposit mass estimates between $1.3\pm 1.1\times10^9$ and 5.7×10^9 kg. Moreover, SFA-based time-averaged mass eruption rates and DRE volume eruption rates from the 3 remote sensors are in agreement with other independent estimates, available in literature.

The analysis of this case study indicates that ground-based radars can be exploited to provide a self-consistent monitoring of the time-varying activity of explosive volcanic eruptions. Polarimetric weather radars can offer the capability of 3-dimensional scanning instruments thus providing a monitoring of the plume dynamics. By combining radar at different wavelengths (23.8 cm at L band, 3.1 cm at X band and 0.9 cm at Ka band) together with lidar monitoring at visible near infrared wavelengths (0.5 and 1.1 μn) to gain a sensitivity to finer particles (e.g., [34]), the total grain size of the tephra plume could be retrieved. Further work is needed to assess the SFA methods, using more explosive eruption cases with a set of instruments at least comparable to the one used in this event and deposit-based volumes. A more robust self-consistent approach to the near-real-time estimates of mass eruption rate should be able to remove some arbitrary assumptions in the SFA formulation (e.g. crater geometry) by exploiting different methodologies and multiple sensor data.

ACKNOWLEDGMENT

The work was carried out in the frame of the H2020-INFRAIA-2016-2017 EUROVOLC project whose team is acknowledged. The VOLDORAD-2B radar of OPGC on Etna is operated in close collaboration with INGV-OE under the responsibility of M. Coltelli, who is deeply acknowledged. VOLDORAD-2B processed data are made available by OPGC in the framework of EPOS [17]. We also thank the Italian Department of Civil Protection (DPC, Italy) for the provision of the X-band radar data.

REFERENCES

[1] Andronico, D., Scollo S., and Cristaldi A., Unexpected hazards from tephra fallouts at Mt Etna: The 23 November 2013 lava fountain, *J. Volcanology and Geothermal Res.*, vol. 304, pp. 118–125, 2015

[2] Behncke, B., S. Falsaperla, and E. Pecora, Complex magma dynamics at Mount Etna revealed by seismic, thermal, and volcanological data, *J. Geophys. Res.*, vol. 114, B03211, doi: 10.1029/2008JB005882, 2009.

[3] Bonaccorso, A., S. Calvari, A. Linde, and S. Sacks, Eruptive processes leading to the most explosive lava fountain at Etna volcano: The 23 November 2013 episode, *Geophys. Res. Lett.*, vol. 41, 4912–4919, doi:10.1002/ 2014GL060623, 2014.

[4] Bonadonna, C., R. Genco, M. Gouhier, M. Pistolesi, R. Cioni, F. Alfano, A. Hoskuldsson, and M. Ripepe, Tephra sedimentation during the 2010 Eyjafjallajokull eruption (Iceland) from deposit radar and satellite observations. *J. Geophys. Res.*, vol. 116, B12202, http://dx.doi.org/10.1029/2011JB008462, 2011.

[5] Bonadonna C, A. Folch, S. Loughlin, and H. Puempel, Future developments in modelling and monitoring of volcanic ash clouds: outcomes from the first IAVCEI-WMO workshop on ash dispersal forecast and civil aviation, *Bull Volcanol*, vol. 74, 1-10. doi: 10.1007/s00445-011-0508, 2012.

[6] Büttner, R, B. Zimanowski, and H. Röder, Short time electrical effects during volcanic eruptions: experiments and field measurements. *J Geophys Res*, vol. 105, 2819–2828. doi: 10.1029/1999JB900370, 2000.

[7] Calvari S., G. G. Salerno, L. Spampinato, M. Gouhier, A. La Spina, E. Pecora, A. J. L. Harris, P. Labazuy, E. Biale, and E. Boschi, An unloading foam model to constrain Etna's 11–13 January 2011 lava fountaining episode, *J. Geophys. Res.*, vol. 116, B11207, doi: 10.1029/2011JB008407, 2011.

[8] Carbone D., L. Zuccarello, A. Messina, S. Scollo and H. Rymer, "Balancing bulk gas accumulation and gas output before and during lava fountaining episodes at Mt. Etna", Nature 2015, Scientific Reports | 5:18049 | DOI: 10.1038/srep18049, 2015.

[9] Casadeval, T. J., Volcanic ash and aviation safety, *U.S. Geol. Surv. Bull.*, 2047, 450–469, 1994.

[10] Coltelli,M., L. Miraglia, and S. Scollo (2008), Characterization of shape and terminal velocity of tephra particles erupted during the 2002 eruption of Etna volcano, Italy, Bull. Volcanol., doi:10.1007/s00445-007-0192-8.

[11] Corradini, S., M. Montopoli, L. Guerrieri, M. Ricci, S. Scollo, L. Merucci, F.S. Marzano, S. Pugnaghi, M. Prestifilippo, L.J. Ventress, R.G. Grainger, E. Carboni, G. Vulpiani, and M. Coltelli, A multi-sensor approach for volcanic ash cloud retrieval and eruption characterization: The 23 November 2013 Etna lava fountain, *Remote Sens.*, vol. 8 (1), 58; doi:10.3390/rs8010058, 2016.

[12] Corsaro R.A., D. Andronico, B. Behncke, S. Branca, T. Caltabiano, F. Ciancitto, A. Cristaldi, E. DeBeni, A. La Spina, L. Lodato, L. Miraglia, M. Neri, G. Salerno, S. Scollo, and G. Spata, "Monitoring the December 2015 summit eruptions of Mt. Etna (Italy): Implications on eruptive dynamics", J. Volcanol. Geotherm. Res, http://dx.doi.org/10.1016/j.jvolgeores.2017.04.018, 2017.

[13] Crouch, J. F., N. Pardo, and C. A. Miller (2014), Dual polarisation C-band weather radar imagery of the 6 August 2012 Te Maari Eruption, Mount Tongariro, New Zealand, J. Volcanol. Geotherm. Res., 286, 415–436, doi:10.1016/j.jvolgeores.2014.05.003.

[14] Degruyter W. and C. Bonadonna, "Improving on mass flow rate estimates of volcanic eruptions," Geophys. Res. Lett., vol. 39, n. 16, L16308, 2012.

[15] Delle Donne, D. and M. Ripepe, High-frame rate thermal imagery of Strombolian explosions: Implications for explosive and infrasonic source dynamics, *J. Geophys. Res.*, vol. 117, B09206, doi:10.1029/2011JB008987, 2012.

[16] Donnadieu, F., Volcanological applications of Doppler radars: A review and examples from a transportable pulse radar in L-band, Bech and Chau, Eds., InTech, 409–446, 2012.

[17] Donnadieu F., Freville P., Rivet S., Hervier C., Cacault P., "The Volcano Doppler radar data base of Etna (VOLDORAD 2B)". Université Clermont Auvergne CNRS. http://wwwobs.univ-

bpclermont.fr/SO/televolc/ voldorad/ bddtr.php, doi: 10.18145/VOLDORAD.ETNA.2009, 2015.
[18] Donnadieu, F., P. Freville, C. Hervier, M. Coltelli, S. Scollo, M. Prestifilipo, S. Valade, S. Rivet, and P. Cacault, Near source Doppler radar monitoring of tephra plumes at Etna, *J. Volcanol. Geotherm. Res.*, 312, 26–39, 2016.
[19] Dürig, T., M. T. Gudmundsson, S. Karmann, B. Zimanowski, P.O. Dellino, M. Rietze and R. Büttner, Mass eruption rates in pulsating eruptions estimated from video analysis of the gas thrust-buoyancy transition a case study of the 2010 eruption of Eyjafjallajökull, Iceland, *Earth, Planets and Space*, vol. 67, 180, doi: 10.1186/s40623-015-0351-7, 2015.
[20] Freret-Lorgeril V., F. Donnadieu, S. Scollo, A. Provost, P. Fréville, Y. Guéhenneux, C. Hervier, M. Prestifilippo and M. Coltelli, "Mass Eruption Rates of Tephra Plumes During the 2011–2015 Lava Fountain Paroxysms at Mt. Etna From Doppler Radar Retrievals", Front. Earth Sci., vol. 6:73. doi: 10.3389/feart.2018.00073, 2018.
[21] Gerst, A, M. Hort, R.C. Aster, J.B. Johnson, and P.R. Kyle, The first second of volcanic eruptions from the Erebus volcano lava lake, Antarctica—energies, pressures, seismology, and infrasound, *J. Geophys Res*, vol. 118, 3318–3340. doi:10.1002/jgrb.50234, 2013.
[22] Gouhier M., J. Eychenne, N. Azzaoui, A. Guillin, M. Deslandes, M. Poret, A. Costa and P., Husson "Low efciency of large volcanic eruptions in transporting very fine ash into the atmosphere", Nature Scientific Reports, vol. 9, 1449 - https://doi.org/10.1038/s41598-019-38595-7, 2019.
[23] Harris, D. M., and W. I. Rose (1983), Estimating particle sizes, concentrations, and total mass of ash in volcanic clouds using weather radar, *J. Geophys. Res.*, 88(C15), 10,969–10,983.
[24] Hort M., R. Seyfried, and M. Vöge, "Radar Doppler velocimetry of volcanic eruptions: Theoretical considerations and quantitative documentation of changes in eruptive behaviour at Stromboli volcano, Italy," Geophys. J. Int., vol. 154, no. 2, pp. 515–532, Aug. 2003.
[25] Kaminski E., S. Tait, F. Ferrucci, M. Martet, B. Hirn, and P. Husson, Estimation of ash injection in the atmosphere by basaltic volcanic plumes: The case of the Eyjafjallajokull 2010 eruption, *J. Geophys. Res.*, 116, B9, Art. no. B00C02, 2011.
[26] Marzano, F. S., G. Vulpiani, and W. I. Rose, Microphysical characterization of microwave radar reflectivity due to volcanic ash clouds, *IEEE Trans. Geosci. Remote Sens*., vol. 44, 313–327, 2006.
[27] Marzano, F.S., S. Barbieri, G. Vulpiani and W.I. Rose, Volcanic cloud retrieval by ground-based microwave weather radar, *IEEE Trans. Geosci. Rem. Sens.*, vol. 44, n.11, pp. 3235-3246, 2006.
[28] Marzano, F. S., S. Marchiotto, S. Barbieri, C. Textor, and D. Schneider, Model-based weather radar remote sensing of explosive volcanic ash eruption, *IEEE Trans. Geosci. Remote Sens*., vol. 48, 3591–3607, 2010.
[29] Marzano, F.S., E. Picciotti, G. Vulpiani and M. Montopoli, "Synthetic Signatures of Volcanic Ash Cloud Particles from X-band Dual-Polarization Radar", *IEEE Trans. Geosci. Rem. Sens*., ISSN: 0196-2892, vol. 50, pp. 193-211, 2012.
[30] Marzano, F.S., E. Picciotti, G. Vulpiani, M. Montopoli, Inside Volcanic Clouds: Remote Sensing of Ash Plumes Using Microwave Weather Radars, *Bull. Am. Met. Soc.*, pp. 1567-1586, 2013.
[31] Marzano, F.S., E. Picciotti, S. Di Fabio, M. Montopoli, L. Mereu, W. Degruyter, C. Bonadonna, and M. Ripepe, "Near-Real-Time Detection of Tephra Eruption Onset and Mass Flow Rate Using Microwave Weather Radar and Infrasonic Arrays", *IEEE Trans. Geosci. Remote Sens*, vol. 54 (11), 6292-6306, doi: 10.1109/TGRS.2016.2578282, 2016.
[32] Mastin, L. G. et al., A multidisciplinary effort to assign realistic source parameters to models of volcanic ash-cloud transport and dispersion during eruptions, *J. Volcanol. Geothermal Res.*, vol. 186, 1/2, 10–21, 2009.
[33] Mereu, L., F.S. Marzano, M. Montopoli, and C. Bonadonna, Retrieval of Tephra Size Spectra and Mass Flow Rate From C-Band Radar During the 2010 Eyjafjallajökull Eruption, Iceland, *IEEE Trans. Geosci. Remote Sens*, doi: 10.1109/TGRS.2015.2427032, 2015.
[34] Mereu L., S. Scollo, S. Mori, A. Boselli, G. Leto and F.S. Marzano, "Maximum-Likelihood Retrieval of Volcanic Ash Concentration and Particle Size From Ground-Based Scanning Lidar", *IEEE Trans. Geosci. Remote Sens*, doi: 10.1109/TGRS.2018.2826839, 2018.
[35] Montopoli, M., G. Vulpiani, D. Cimini, E. Picciotti, and F.S. Marzano, Interpretation of observed microwave signatures from ground dual polarization radar and space multi frequency radiometer for the 2011 Grímsvötn volcanic eruption, *Atmos. Meas. Tech.*., vol. 7, 537–552, 2014.
[36] Montopoli, M., Velocity profiles inside volcanic clouds from three-dimensional scanning microwave dual-polarization Doppler radars, *J. Geophys. Res. Atmos*., vol. 121, 7881–7900, doi: 10.1002/ 2015JD023464, 2016.
[37] Parfitt A. E., A discussion of the mechanisms of explosive basaltic eruptions, *J. Volcanology and Geothermal Research*, vol. 134, 77–107, 2004.
[38] Poret M., S. Corradini, L. Merucci, A. Costa, D. Andronico, M. Montopoli, G. Vulpiani, and V. Freret-Lorgeril, Reconstructing volcanic plume evolution integrating satellite and ground-based data: Application to the 23rd November 2013 Etna eruption, *Atmos. Chem. Phys.*, https://doi.org/10.5194/acp-2017-1146, 2018.
[39] Ripepe, M., C. Bonadonna, A. Folch, D. Delle Donne, G. Lacanna, and B. Voight, Ash-plume dynamics and eruption source parameters by infrasound and thermal imagery: The 2010 Eyjafjallajokull eruption, *Earth Planet. Sci. Lett*., 366, 112–121, doi: 10.1016/j.epsl.2013.02.005, 2013.
[40] Saunderson, H. C., Equations of motion and ballistic paths of volcanic ejecta, Computers & Geosciences, vol. 34, n. 7, pp. 802-814, https://doi.org/10.1016/j.cageo.2007.10.004, 2008.
[41] Scollo, S., Prestifilippo, M., Spata, G., D'Agostino, M., Coltelli, M.. "Monitoring and forecasting Etna volcanic plumes", *Natural Hazards and Earth System Sciences*, vol. 9, 1573-1585, 2009.
[42] Scollo, S., M. Prestifilippo, E. Pecora, S. Corradini, L- Merucci, G. Spata, and M. Coltelli, Eruption column height estimation of the 2011-2013 Etna lava fountains, *Annals of Geophys.*, vol. 57, 2, S0214. doi:10.4401/ag-6396, 2014.
[43] Scollo, S., Boselli, A., Coltelli, M., Leto, G., Pisani, G., Prestifilippo, M., Spinelli, N., Wang, X.. "Volcanic ash concentration during the 12 August 2011 Etna eruption", Geophysical Research Letters, 10.1002/2015GL063027, 2015.
[44] Sparks R., The dimensions and dynamics of volcanic eruption columns, *Bull. Volcanol.*, vol. 48, 1, pp. 3–15, 1986.
[45] Sparks, R. S. J., M. I. Bursik, S. N. Carey, J. S. Gilbert, L. S. Glaze, H. Sigurdsson, and A. W. Woods, *Volcanic plumes*. New York, NY, USA: Wiley, 1997.
[46] Stephen R., J. Sparks and Herbert E. Huppert, "Density changes during the fractional crystallization of basaltic magmas: fluid dynamic implications", Contrib Mineral Petrol, vol. 85, pp. 300-309, 1984.
[47] Taddeucci, J., P. Scarlato, A. Capponi, E. Del Bello, C. Cimarelli, D.M. Palladino, and U. Kueppers, High-speed imaging of Strombolian explosions: the ejection velocity of pyroclasts. *Geophys Res Lett*, vol. 39, L02301. doi: 10.1029/ 2011GL050404, 2012.
[48] Ulivieri G., M. Ripepe, and E. Marchetti, "Infrasound reveals transition to oscillatory discharge regime during lava fountaining: Implication for early warning," *Geophys. Res. Lett.*, vol. 40, n. 12, pp. 3008–3013, Jun. 2013.
[49] Valade, S, A.J.L. Harris, and M. Cerminara, Plume ascent tracker: interactive Matlab software for analysis of ascending plumes in image data. *Comput Geosci*, vol. 66, 132–144. doi: 10.1016/j.cageo.2013.12.015, 2014.
[50] Vulpiani, G., M. Ripepe, and S. Valade, Mass discharge rate retrieval combining weather radar and thermal camera observations, *J. Geophys. Res. Solid Earth*, 121, doi: 10.1002/2016JB013191, 2016.
[51] Wilson, L., R. S. J. Sparks, T. C. Huang, and N. D. Watkins, The control of volcanic column heights by eruption energetics and dynamics, J. Geophys. Res., 83(B4), 1829–1836, 1978.
[52] Wilson, L., and G. P. L. Walker, Explosive volcanic eruptions—VI. Ejecta dispersal in plinian eruptions: The control of eruption conditions and atmospheric properties, Geophys. J. R. Astron. Soc., 89, 657–679, 1987.

Frank S. Marzano [S'89-M'99-SM'03-F'16] received the Laurea degree (*cum laude*) in Electrical Engineering (1988) and the Ph.D. degree (1993) in Applied Electromagnetics both from the University of Rome "La Sapienza", Italy. In 1992 he was a visiting scientist at Florida State University, Tallahassee, FL. During 1993 he collaborated with the Institute of Atmospheric Physics, National Council of Research (CNR), Rome, Italy. From 1994 till 1996, he was with the Italian Space Agency, Rome, Italy, as a post-doctorate researcher. After being a lecturer at the University of Perugia, Italy,

in 1997 he joined the Department of Electrical Engineering, University of L'Aquila, Italy teaching courses on electromagnetic fields as Assistant Professor. In 1999 he was at Naval Research Laboratory, Monterey, CA, as a visiting scientist. In 2002 he got the qualification to Associate Professorship and has co-founded Center of Excellence on Remote Sensing and Hydro-Meteorological Modeling (CETEMPS), L'Aquila. In 2005 he finally joined the Dept. of Information engineering, Electronics and Telecommunications, Sapienza Univ. of Rome, Italy where he is presently a full professor teaching courses on antennas, propagation and remote sensing. Since 2007 he has been vice-director of CETEMPS of the University of L'Aquila, Italy where he was nominated director on March 2013. His current research concerns passive and active remote sensing of the atmosphere from ground-based, airborne, and space-borne platforms and electromagnetic propagation studies.

Dr. Marzano has published more than 150 papers on refereed international journals, more than 30 contributions to international Book chapters and more than 300 extended abstract on international and national congress proceedings. He was the Editor of 2 books. From January 2004 till June 2014 he has been acting as an *Associated Editor* of IEEE Geoscience Remote Sensing Letters (GRSL) and since mid 2014 he is *Associated Editor* of IEEE Transactions on Geoscience and Remote Sensing (TGRS). In 2005 and 2007 he has been Guest Co-Editor of the MicroRad04 and MicroRad06 Special Issues for IEEE-TGRS. Since January 2011 he is Associate Editor of the journal EGU Atmospheric Measurements Techniques. Dr. Marzano is Fellow of RMetS (Royal Meteorological Society) since 2012 and Fellow of IEEE since 2015.

Luigi Mereu received the B.Sc. in telecommunication engineering and the M.Sc. degree in telecommunication engineering in 2007 and 2012, respectively, and the PhD in remote sensing in 2016, all from Sapienza University of Rome, Italy. In 2012 he joined the Department of Information Engineering at Sapienza University of Rome, Italy and the Centre of Excellence CETEMPS in L'Aquila to cooperate on radar remote sensing of volcanic ash clouds within the Ph.D. program. He was involved within the FUTUREVOLC European project started in 2012, in the Aphorism project started in 2014 and recently in EUROVOLC. He received the IEEE GRS South Italy award for the Best Master Thesis in remote sensing in 2012.

Simona Scollo was awarded a degree (with Hons.) in Physics (2002) at the University of Catania and a Ph.D. degree (2006) in "Physical Modelling for Environmental Protection" at the Università Alma Mater Studiorum of Bologna. She is volcanologist at the Istituto Nazionale di Geofisica e Vulcanologia, Osservatorio Etneo. Her current research focuses on the analysis of the dispersal and fallout processes of eruptive plumes during explosive eruptions; calibration, sensitivity analysis and uncertainty estimation of ash dispersal models; laboratory and field experiments; development of a multidisciplinary system for the detection and monitoring of volcanic plumes and analysis of explosive activity using different remote sensing techniques (e.g. radar, lidar, satellites).

She coordinated several projects and one of them, the VAMOS SEGURO project, was selected in 2012 as a "best practice" among several European Cooperation Projects. In 2011, she obtained the Rittmann medal for young researchers in volcanology and in 2010 the paper Scollo et al. (2010) was selected for the "AGU Research Spotlight".

Franck Donnadieu completed a Ph.D. degree in Volcanology (2000) at the Université Clermont II (France) followed by a NSF post-doctoral fellowship at Penn State University (USA). He then spent one year at the Observatoire de Physique du Globe de Clermont-Ferrand to specialize in sounding of volcanic explosive eruptions using dedicated transportable radars. Since 2002, he is Physicien adjoint at OPGC (Lab. Magmas et Volcans), Université Clermont Auvergne (France) and was awarded the HDR diploma in 2017. As part of the french SNOV (CNRS-INSU), he is in charge of a unique service (VOLDORAD) dedicated to volcanological Doppler radars comprising four instruments (3 UHF, 1 mm-wave) involved in 10 campaigns, one radar being permanently monitoring Etna in collaboration with INGV-OE. Franck Donnadieu has devoted most of his research to better quantifying volcanic jets and plumes dynamics and source parameters from radar remote sensing. He was coordinator at UCA of the European MED-SUV program (2013-2016) and led the ash plume radar project of the ClerVolc Laboratory of excellence (2015-2018). He obtained three PEDR and one UCA awards for scientific excellence. He is also teaching courses in geophysics.
Formerly a member of the French CNAP and SNOV national committees, Dr. Donnadieu is also a member of IAVCEI, of the scientific board on Soufrière de Guadeloupe and of the OPGC administration board.

Costanza Bonadonna is full professor at the Department of Earth Sciences, University of Geneva and the head of the CERG-C program http://www.unige.ch/sciences/terre/CERG-C/. She received her undergraduate Geology degree at the University of Pisa, Italy, and she completed her PhD at the University of Bristol, UK. She was then awarded the position of Young Investigator at the University of Hawaii and she was later appointed the position of Assistant Professor at the University of South Florida, USA. Other awards include the President's Award of the Geological Society of London (2001), the IAVCEI Outstanding Recent Graduate (2004), the Outstanding Woman in Science Award of the Geological Society of America (2004) and the USF Outstanding Faculty Research Achievement Award (2005). Costanza Bonadonna has devoted most of her research to modelling sedimentation from volcanic plumes, exploring new methodologies for the characterization of tephra-fall deposits and developing probabilistic analysis for the assessment of tephra-fall hazards.

LIST OF TABLES

Table. List of main symbols

Name	Symbol	Units
Tephra concentration	C_t	kg/m^3
Tephra particle density	ρ_t	kg/m^3
Magma density	ρ_m	kg/m^3
Eruptive mixture density	ρ_x	kg/m^3
Gas density	ρ_g	kg/m^3
Gas volumetric fraction	f_g	adimensional
Airborne particle volumetric fraction	f_N	adimensional
Vertical exit velocity	v_{ex}	m/s
Vent surface	S_v	m^2
Incandescent region top height	H_{IR}	m
Top-plume height	H_{TP}	m
Mass eruption rate at time *t*	$Q_M(t)$	kg/s
Volumetric eruption rate at time *t*	$Q_V(t)$	m^3/s
Integrated erupted mass at time *t*	$M_I(t)$	kg
Total erupted mass (TEM) during the event	M_T	kg
Total erupted volume during the event	V_T	m^3
Eruption event duration	Δt	s
Time-averaged mass eruption rate (MER)	$\bar{Q}_M$	kg/s
Time-averaged volumetric eruption rate	$\bar{Q}_V$	kg/m^3

Table I. Total erupted mass (in kg) for the Etna eruption on 23 Nov. 2013 between 09:30 and 10:40 UTC, derived from literature (rows a, b, c_1 and c_2) as well as applying the parametric models of Degruyter and Bonadonna (DB12) and Mastin (MA09) (rows d and e), from TIC data, X-band MWR and L-band VDR (rows f, g and h, respectively) and X-band MWR (row i), together with their uncertainties.

Source	Total erupted mass (kg)
a) from Andronico et al., 2015 (field collection)	$1.3 \pm 1.1\times10^9$
b) from Corradini et al., 2015 (satellite data)	$3.0 \pm 1.0\times10^9$
c1) from Poret et al., 2018 (satellite-radar-model TGSD)	5.7×10^9
c2) from Poret et al., 2018 (field grain size)	1.6×10^9
d) TPA-DB12 using Degruyter-Bonadonna, 2012 (mean vel.=20 m/s)	$4.3\pm1.0\times 10^9$
e) TPA-MA09 using Mastin et al., 2009	$1.7\pm0.4\times 10^9$
f) SFA using TIC data	$4.7\pm1.3\times10^9$
g) SFA using X-band MWR	$3.9\pm1.0\times10^9$
h) SFA using L-band VDR	$4.2\pm1.0\times10^9$
i) MCA using X-band MWR	$3.9\pm0.9\times10^9$

Table II. Time-averaged mass eruption rate (in kg/s), time-average volumetric eruption rate (in m^3/s) and total erupted volume (in m^3), derived from SFA for each sensor used in this case study. The first and second number in each cell of the first 3 rows are the estimates assuming in (7) and (8) either ρ_m=2700 kg/m^3 and Δt=4200 s (lower value) or ρ_m=2500 kg/m^3 and Δt=3000 s (larger value), respectively. The last 3 rows show data available from literature in [1], [3] and [20].

Method and data source	Time-averaged mass eruption rate (kg/s)	Time-averaged volumetric eruption rate (m^3/s)	Total erupted volume (m^3)
SFA using TIC data	$1.1\times10^6 – 1.6\times10^6$	415.0 – 627.4	1.7×10^6 - 1.9×10^6
SFA using X-band MWR	$0.9\times10^6 – 1.3\times10^6$	347.6 – 525.6	1.4×10^6 - 1.6×10^6
SFA using L-band VDR	$0.9\times10^6 – 1.4\times10^6$	365.5 – 557.1	1.5×10^6 - 1.7×10^6
MCA using X-band MWR	$0.9\times10^6 – 1.3\times10^6$	347.7 – 525.6	$1.5\times10^6 – 1.6\times10^6$
Andronico et al., 2015 JVGR [1]	$0.5\pm0.4\times10^6$	-	-
Bonaccorso et al., 2014 GRL [3]	-	360.0	1.6×10^6
Freret-Lorgeril et al., 2018 Frontiers [20]	$3.98\times10^5 – 3.26\times10^6$ (climax)	147 – 1207 (climax)	1.7×10^6

LIST OF FIGURES

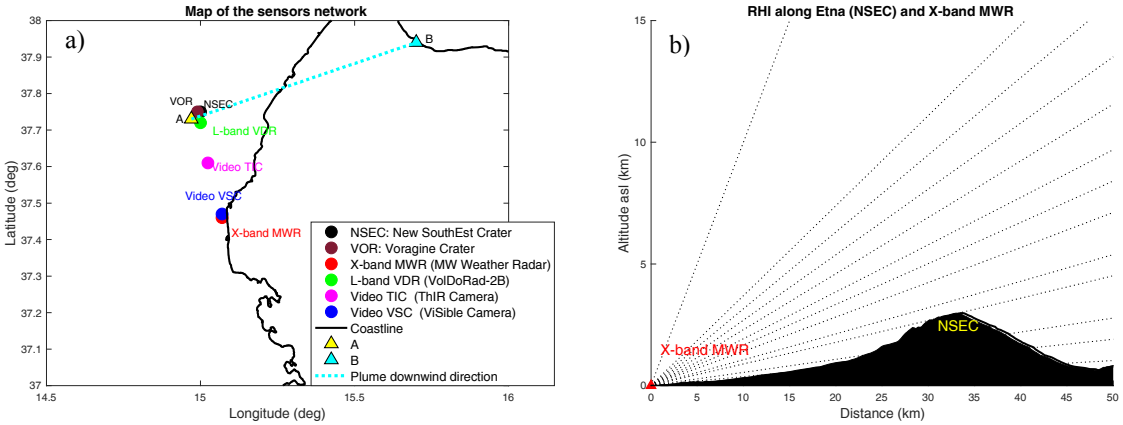

Figure 1. a) Map locating all available remote sensors around the Mt. Etna site in this study. b) Vertical profile showing the range-height index (RHI) of the X-band radar (MWR) between the MWR site at the "Fontanarossa" airport in Catania (Italy) and the New South- East Crater (NSEC).

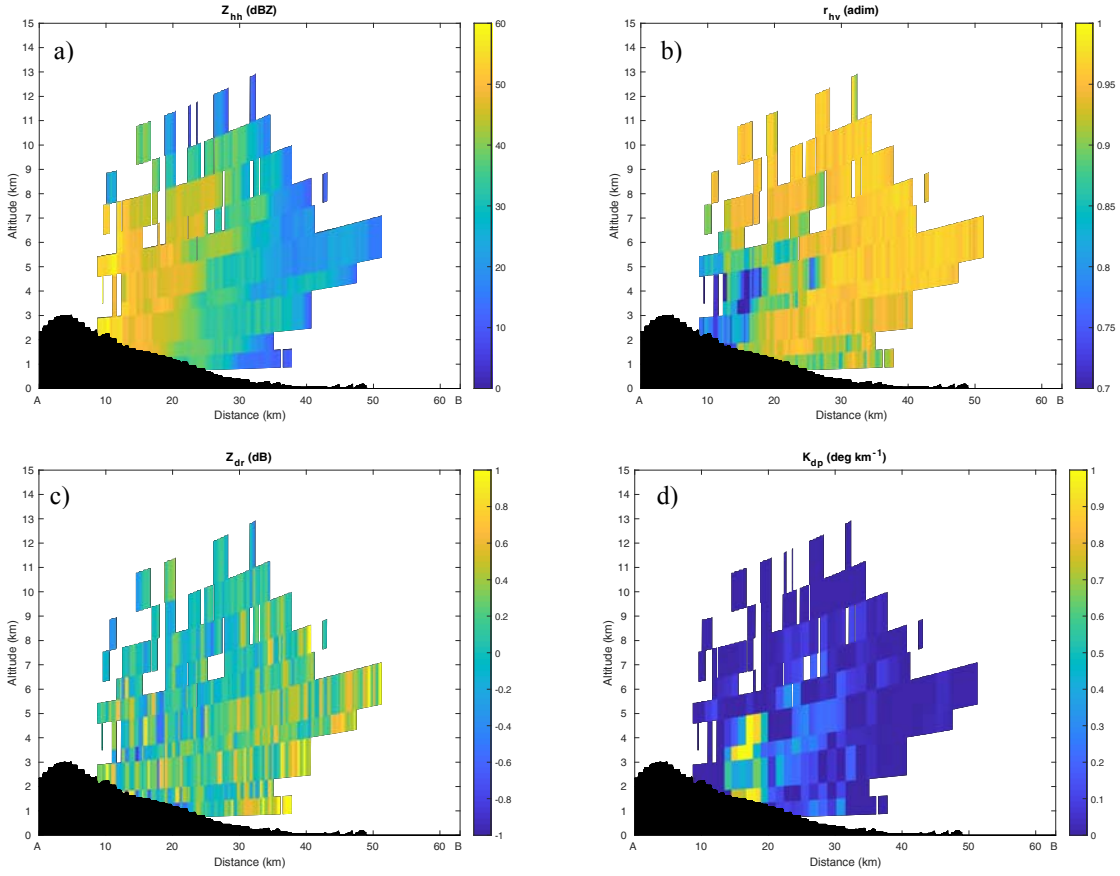

Figure 2. Retrieval of Etna explosive activity of 23 November 2013 at 10:00 UTC. a) Vertical profile of the radar reflectivity factor Z_{hh} (dBZ) of X-band radar (MWR) along the A-B line (see Fig. 1a) connecting the vent to the plume reflectivity peak. b) Same as in a), but for the copolar cross-correlation coefficient r_{hv} (adim). c) Same as a), but for the differential reflectivity Z_{dr} (dB). d) Same as in a), but for the differential phase shift K_{dp} (adim).

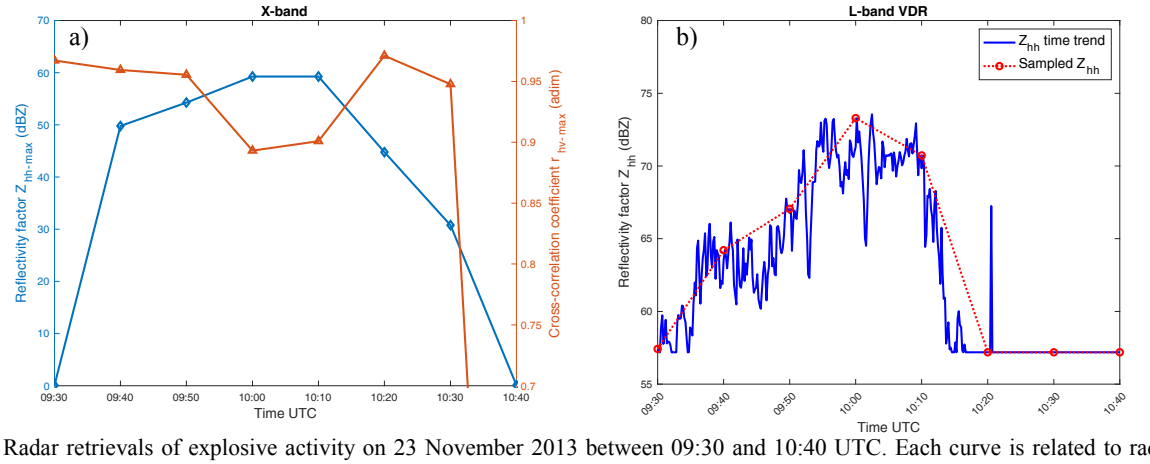

Figure 3. Radar retrievals of explosive activity on 23 November 2013 between 09:30 and 10:40 UTC. Each curve is related to radar fourth range bin (elevation) near to the summit crater. a) Horizontally-polarized reflectivity factor Z_{hh} (dBZ) and the cross-correlation coefficient r_{hv} [adim], both derived from the X-band radar (MWR) sampled every 10 minutes (and then linearly interpolated). b) Radar reflectivity factor Z_{hh} (dBZ) of the L-band VOLDORAD-2B (VDR) measured near the emission source, as provided by VDR at about 17 s sampling (blue line) and its linearly interpolated trend (red line) with samples every 10 minutes.

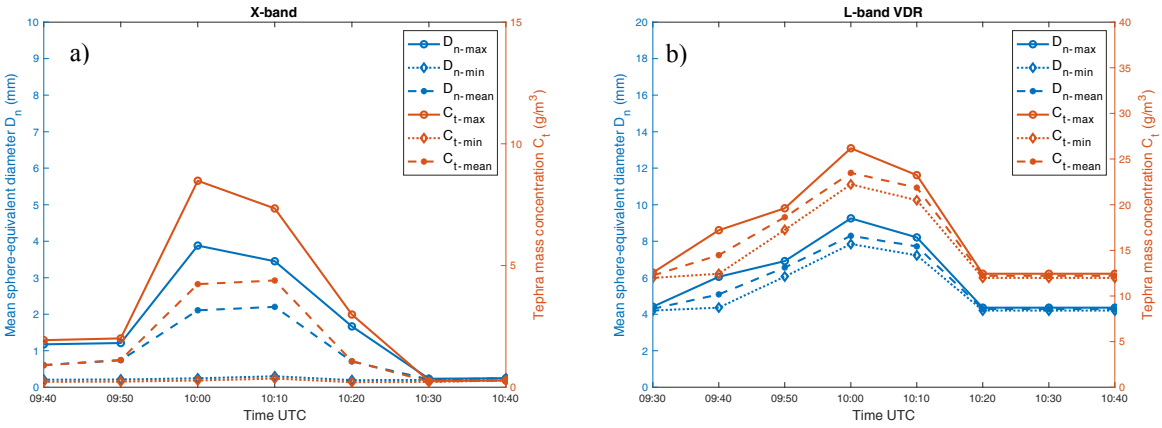

Figure 4. Radar retrievals of 23 November 2013 Etna volcanic plume between 09:30 and 10:40 UTC sampled every 10 minutes (and then linearly interpolated). Each curve is sampled every 10 minutes, as imposed by the MWR operational schedule. Data near to the NSEC are relative to fourth elevation angle of MWR and to the third or fourth range-bin of VDR. a) VARR-based retrievals of maximum and minimum of tephra mass concentration C_t (g/m^3) and mean sphere-equivalent diameter D_n (mm), derived from the X-band radar (MWR). b) Same as in the left panel, but derived from the L-band radar (VDR).

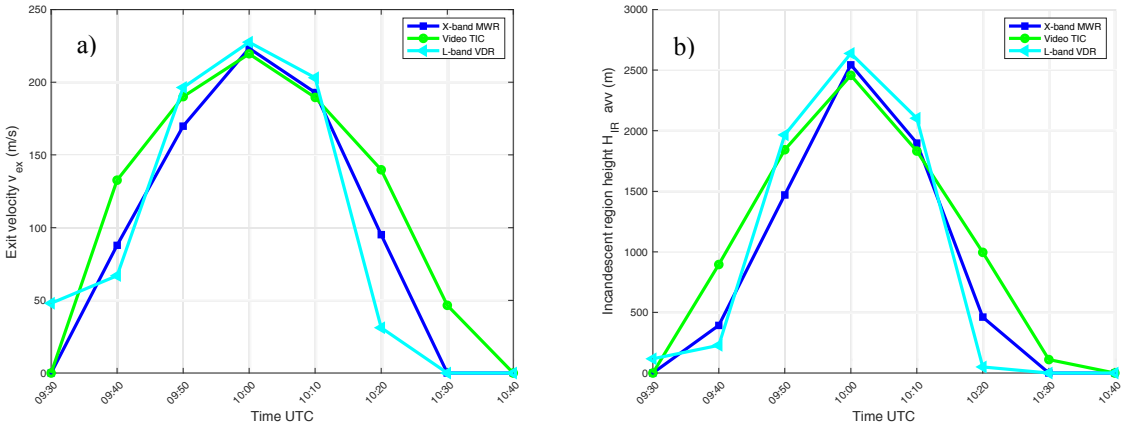

Figure 5. Radar and video retrievals of the Etna volcanic plume on 23 November 2013 between 09:30 and 10:40 UTC sampled every 10 minutes (and then linearly interpolated). a) Estimates of the exit velocity v_{ex} (m/s), derived from X-band radar (MWR), L-band VOLDORAD-2 (VDR) and video thermal-infrared camera (TIC). Note that v_{ex} is directly extracted from VDR, whereas obtained from MWR and TIC by inverting the estimate of the incandescent region height H_{IR} through the Torricelli equation b) Estimates of the incandescent region height H_{IR} (m) derived from three sensors MWR, TIC and VDR. In contrast H_{IR} is directly extracted from MWR and TIC, and obtained from VDR by inverting the estimate of the exit velocity v_{ex} through the Torricelli equation.

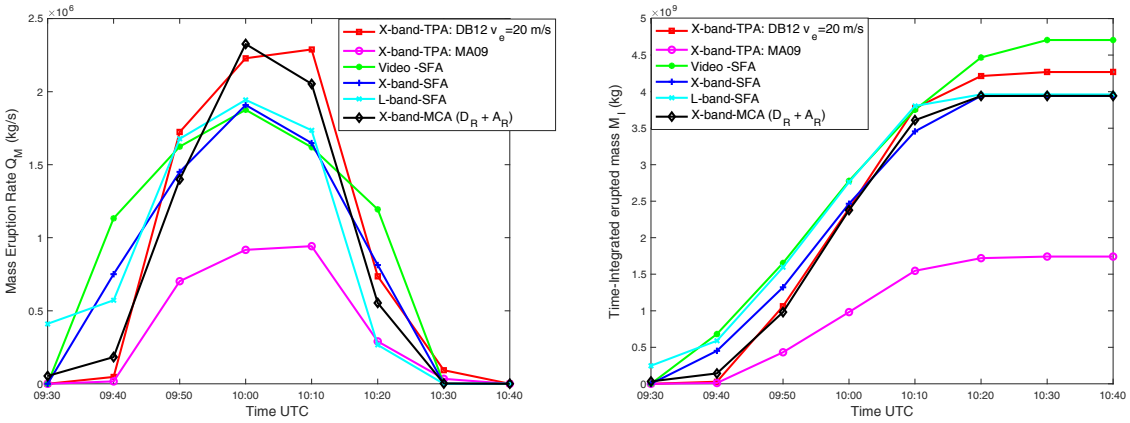

Figure 6. Etna explosive event on 23 Nov. 2013 between 09:30 and 10:40 UTC sampled every 10 minutes (and then linearly interpolated). a) Estimates of the mass eruption rate $Q_M(t)$ (kg/s) as a function of time t, derived from: (i) TPA (Top-plume approach) methods, i.e. using the top-plume altitude H_{TP} retrieved from the X-band radar within the parametric relationship of Degruyter and Bonadonna (DB12) (setting a mean wind velocity of 20 m/s) and Mastin et al. 2009 (MA09); (ii) SFA (Surface flux approach) methods, i.e. using the flux equation and the exit velocity estimated from the video thermal-infrared camera (TIC), X-band microwave radar (MWR) and L-band VOLDORAD-2 radar (VDR); (iii) MCA (Mass continuity approach) method, i.e using the mass continuity equation. Each curved is sampled every 10 minutes, the minimum common sampling time imposed by the MWR operational schedule. (Right panel, b) Time-Integrated erupted mass $M_I(t)$ (kg) as a function of time t as derived from the same techniques as listed in the left panel. The last value of $M_I(t)$ at 10:40 UTC represents the Total erupted mass M_T.

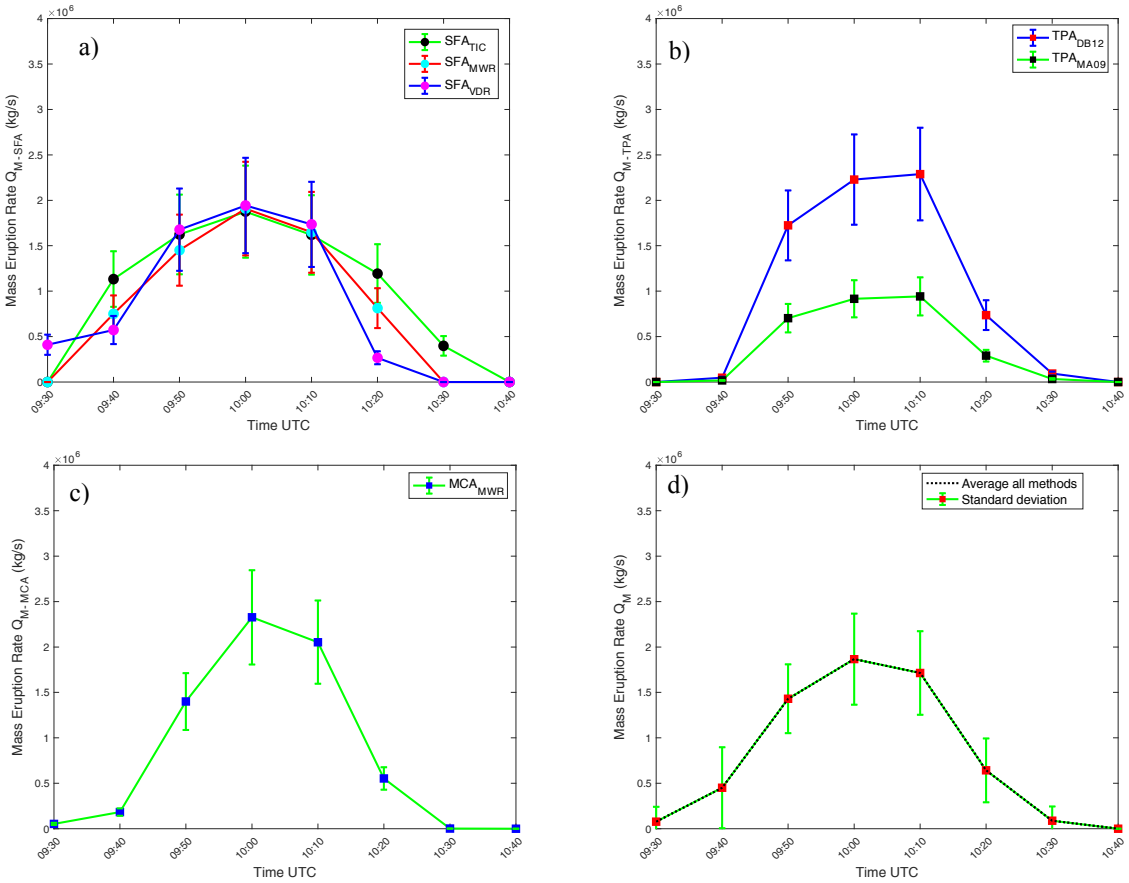

Figure 7. Estimated mass eruption rate $Q_M(t)$, similarly to Fig. 6 (a), but with the representation of their own uncertainty (indicated by vertical bars) for SFA methods (a), TPA methods (b) and MCA method (c). In panel (d) the total mean of mass eruption rate estimates, derived from all SFA, TPA, and MCA methods, together with the associated standard deviation, are shown.